Chapter 10
Applications of Ion Induction Accelerators

John J. Barnard and Richard J. Briggs

As discussed in Chap. 9, the physics of ion induction accelerators has many commonalities with the physics of electron induction accelerators. However, there are important differences, arising because of the different missions of ion machines relative to electron machines and also because the velocity of the ions is usually non-relativistic in these applications. The basic architectures and layout reflects these differences. In Chaps. 6, 7, and 8 a number of examples of electron accelerators and their applications were given, including machines that have already been constructed. In this chapter, we give several examples of potential uses for ion induction accelerators. Although, as of this writing, none of these applications have come to fruition, in the case of heavy ion fusion (HIF), small scale experiments have been carried out and a sizable effort has been made in laying the groundwork for such an accelerator. A second application, using ion beams for study of High Energy Density Physics (HEDP) or Warm Dense Matter (WDM) physics will soon be realized and the requirements for this machine will be discussed in detail. Also, a concept for a spallation neutron source is discussed in lesser detail.

10.1 Driver for Heavy Ion Fusion (HIF)

To understand the energy, current, and power requirements for a HIF ion induction accelerator, it is useful to start at the target. Consideration of the final focus, which ultimately determines the final spot radius and hence beam intensity, places constraints on the beam brightness, which together with the target requirements, specifies the macro requirements on the beam (such as beam energy, current, and emittance). Working upstream from the final focus, requirements on the accelerator and injector can then be set. In early studies of HIF, RF as well as induction options were considered [1] and indeed RF approaches continue to be pursued [2]. Most of the US research has been focused on induction accelerator approaches to HIF, because of the perceived ability of the induction technology to produce pulses of

---

J.J. Barnard (✉)
Lawrence Livermore National Laboratory, Livermore, CA, USA
e-mail: jjbarnard@llnl.gov

K. Takayama, R.J. Briggs (eds.), *Induction Accelerators*, Particle Acceleration and Detection, DOI 10.1007/978-3-642-13917-8_10,

high peak power affordably. But even with a downselect to induction acceleration many beam and architecture choices remain to be made, such as the ion energy and focusing system, and the number and arrangement of beamlines and induction corelines. In this section, we give three examples of HIF driver concepts, to illustrate some of these possibilities.

10.1.1 Requirements Set by Target Physics

Beams of heavy ions are but one of several possible methods of delivering energy to an inertial confinement fusion (ICF) target (see e.g. [3]). Light ions, lasers, "z-pinches," and electrons have also been proposed. ICF targets come in two general varieties: direct drive, where the driver beam illuminates a capsule (containing the fusion fuel) directly, and from all sides, and "indirect drive" where the driver beam heats a "hohlraum," and the hohlraum produces X-rays which illuminate the capsule. In both cases, the heated outer layers of the capsule are ablated outward, driving a fuel shell inward. The inward driven shell compresses the gas fuel within the shell and the shell itself, to the point where the gas reaches the temperature required for fusion of the reactants, and at a density sufficient to stop a significant fraction of the reaction byproducts (in the case of Deuterium-Tritium fuel, alpha-particles), causing "ignition" and "burn" to occur. The implosion of the shell must be isotropic, otherwise hot material will mix with cool material preventing ignition. The use of hohlraums allows the capsule to be illuminated very uniformly, minimizing the seed for Rayleigh-Taylor instability, a possible source of anisotropic implosion. Further the ion beams need not be distributed over four π steradians. Typically, ion beams are directed at two (or a few) radiation converters, which can be located near the ends of, and at various points within, the cylindrical hohlraums. However, the use of a hohlraum is less efficient; more of the energy of a driver pulse is used in heating the hohlraum material, instead of imploding the capsule. Consequently, indirect drive requires the driver to be more efficient in converting "wall-plug" energy into beam energy. Accelerators (and particularly induction accelerators operating at high current) can be highly efficient so indirect direct drive is an option for HIF. Direct drive has also been suggested for HIF, and there has been a recent resurgence of interest in direct drive targets for HIF because of the potential for high gain, low energy targets [4]. However, with direct drive targets in order to achieve uniform illumination the ion beams must illuminate all four π steradians. This may require a final focusing system with beams converging at large angles out of the plane of the accelerator or targets designed such that ion deposition occurs from a limited number of angles, but nevertheless produces uniform compression. If the compression is sufficiently isotropic, the efficient coupling of beam energy into fuel shell kinetic energy can significantly reduce the total energy required by the driver [4].

As the ion mass increases at fixed ion energy, the ion range decreases, and the shorter range of heavier ions allows one to use ions of high energy that can still be stopped within a small range R (roughly the product of mass density ρ and physical stopping distance). Short range (0.015–0.15 g/cm^2) is desired to minimize the amount of material that is heated by the ions. High ion energy is desirable, to minimize the amount of current transported to the target, allowing the use of conventional accelerators and assure focusability. Ultimately, though, high ion energy can translate to high cost and therefore accelerators which optimize acceleration and transport costs must be chosen. Typical parameters for recent HIF targets are: ion range 0.03 g/cm^2, main pulse energy of 0.5–7 MJ, pulse duration of about 2–8 ns, focal spot radius of $\sim$1.8 mm. Recent US designs include distributed radiator target [5], closely coupled targets [6], so-called "hybrid targets" [7, 8], direct drive targets [4], and "fast ignition" targets [9].

10.1.2 Final Focus Limits

Targets driven by heavy ion beams require the ability to focus ion beams onto small spots. Typical systems designs indicate that within the accelerator, the beam radius can be of order centimeters, whereas at the final focal spot on the target, beam radii of order millimeters are required, so radial compression factors of order ten are required. Target gain, and hence the overall cost of electricity is a sensitive function of the final spot radius on target. To get an appreciation of the factors which help determine the spot size, we present here simple models similar to what could be used in a systems code, in which algebraic relations are used to model many aspects of the driver system and to develop a self-consistent model of a heavy ion driven inertial fusion power plant. Because of the sensitivity of spot radius on target gain, careful attention needs to be paid to the part of the model that calculates the spot radius. Recent research has investigated the feasibility of using nearly complete neutralization of the beam in the target chamber in order to remove the effects of space charge (known as neutralized ballistic transport). Neutralized ballistic focusing experiments, analytic calculations, and simulations all point to the possibility of focusing highly neutralized ($> 99\%$) beams.

First we consider constraints on the beam assuming unneutralized ballistic transport to the target. When focusing the beam through a final convergent angle θ, if the beam is not neutralized, space charge is one of the elements that limits the final beam radius. Starting with the envelope equation (see e.g. [10]), we may make an estimate on how much space charge can be focused to a particular spot size.

$$a_x'' + \frac{(\gamma_b\beta_b)'}{(\gamma_b\beta_b)} a_x' + \kappa_x a_x - \frac{2Q}{a_x + a_y} - \frac{\varepsilon_x^2}{a_x^3} = 0. \tag{10.1}$$

After the beam passes through the final focusing element $\kappa_x = 0$, if the spot is circular, $a_x = a_y$, and $\beta_b' = 0$, so that Eq. (10.1) can be integrated, assuming the perveance Q and the emittance ε_x are conserved,

$$\frac{a_x'^2}{2} - Q\ln(a_x) + \frac{\varepsilon_x^2}{2a_x^2} = \frac{a_{x0}'^2}{2} - Q\ln(a_{x0}) + \frac{\varepsilon_x^2}{2a_{x0}^2} \tag{10.2}$$

Here subscript 0 indicates evaluation just outside the final focus element. If we identify the value of a_x at the focus to be r_s, and the convergence angle θ to be $a'_{x0} \simeq a_{x0}/d$ where d is the distance between the last magnet and the final focus, we may rearrange Eq. (10.2) as:

$$\theta^2 = 2Q\ln(\theta d/r_s) + \varepsilon_x^2\left(\frac{1}{r_s^2} - \frac{1}{a_{x0}^2}\right) \tag{10.3}$$

The perveance can be expressed (non-relativistically) as $Q = \lambda/(4\pi\epsilon_0 V)$ where qV is the final ion energy, q is the ion charge, and λ is the line charge density ($\lambda = Q_c/(\beta c \Delta t_f)$), where Q_c is the charge in each beam, βc is the ion velocity and Δt_f is the pulse duration at final focus. The total charge $Q_{c\text{tot}} = N_b Q_c$, where N_b is the total number of beams. If the beams are not neutralized in final focus, Eq. (10.3) can be expressed as a lower limit on the number of beams (by neglecting the emittance term):

$$N_b > \frac{Q_{c\text{tot}}\ln(\theta d/r_s)}{2\pi\epsilon_0\theta^2 V\beta c\Delta t_f} \tag{10.4}$$

For a multi-beam linac with final energy of 4 GeV total charge $Q_{c\text{tot}}$ of 1,650 μC, and convergence angle $\theta = 0.015$ rad, ∼ 220 beams would be required. For the recirculator design of [11] with a total charge $Q_{c\text{tot}}$ in all beams of 400 μC, convergence angle $\theta = 0.03$ rad, and $\beta = 0.3$ (corresponding to 10 GeV), N_b could be as small as 4.

The thermal contribution to spot size places a limit on the normalized emittance ε_N. Again using (10.3) (assuming space charge has been neutralized) a requirement on the emittance may be estimated:

$$\varepsilon_N < \beta\theta r_s = 8\text{ mm-mrad}\left(\frac{\beta}{0.2}\right)\left(\frac{\theta}{0.015}\right)\left(\frac{r_s}{2.5\text{ mm}}\right)$$

Chromatic aberration limits for transport through quadrupole or solenoid lenses place a limit on the momentum spread,

$$\frac{\Delta p}{p} < \frac{r_s}{\alpha_c\theta d} = 3\times10^{-3}\left(\frac{r_s}{2.5\text{ mm}}\right)\left(\frac{0.015}{\theta}\right)\left(\frac{5\text{ m}}{d}\right)\left(\frac{6}{\alpha_c}\right),$$

where d is the distance from target to final focusing magnet, and α_c is a constant depending on magnet layout and type. For quadrupole systems, $\alpha_c \simeq$ 4–6 and for solenoid final optics $\alpha_c = 2$.

Geometric aberrations limit the convergent angle for uncorrected optics, $\theta \lesssim 0.015$ rad (see [12]), although the general scaling for this limit has not been thoroughly explored. Using octupoles [13], it was found that this limit could be relaxed, and designs as large as $\theta = 0.030$ rad have been considered.

The target power requirements place limits on the 3D space coordinates of the beam (pulse length and beam radius r_s) while final focus optics place constraints on the 3D momentum coordinates ($\Delta p/p$, ε_{nx}/r_s, and ε_{ny}/r_s), necessary to reach the spot radius r_s. Additionally because of Liouvilles theorem, the final 6D phase volume occupied by the beam will be at least as large as the initial volume. This constraint can be expressed [14] by a "dilution factor" D, which is a ratio of the initial to final 6D volumes and is a measure of how much room for emittance dilution exists in any particular driver concept:

$$D = \frac{\varepsilon_{Nf}^2 \Delta p_f \ell_f}{\varepsilon_{Ni}^2 \Delta p_i \ell_i} \tag{10.5}$$

Here ℓ_i and ℓ_f are the initial and final bunch lengths of the beam. If we assume the focusing limits on emittance and momentum spread discussed above, for the recirculator [11] (in which $\varepsilon_{Nf} < 8$ mm-mrad, $\varepsilon_{Ni} = 0.5$ mm-mrad, $p_i/p_f = 1.7 \times 10^{-2}$, $\ell_f = 1$ m, $\ell_i = 340$ m, $\Delta p/p_f < 1.4 \times 10^{-3}$, and $\Delta p/p_i \gtrsim 10^{-3}$ from assumed voltage errors in the injector), we find that there is phase-space dilution allowance $D \simeq 62$, which allows for only a factor of 4 growth in phase area in each of the three directions. This relatively small leeway is largely a result of the large initial pulse duration chosen in the recirculator [11], to reduce the number of beams. As one increases the number of beams as in the linac designs the constraint relaxes.

(Note that $D > 1$ is a minimum requirement. If coupling between the transverse and longitudinal directions is not sufficiently strong, the areas of individual phase space projections in each direction (i.e. ε_{Nx}, ε_{Ny}, or Δpl) will individually be non-decreasing, which in some cases can result in a stronger constraint on allowable emittance dilution.) Particle-in-cell simulations are needed to determine the emittance growth through the accelerator (see e.g. [15]).

10.1.3 Accelerator Architectures for Inertial Fusion Energy

Several induction accelerator architectures have been proposed for heavy ion driven Inertial Fusion Energy (IFE) (see e.g. [16–18]). Multiple beam linacs with quadrupolar or solenoidal focusing have been proposed to transport and accelerate the high line-charge densities required. Linacs with both high and low ion charge-to-mass ratio have been explored, with significantly different architectures, arising mainly from the different accumulated ion voltage, and current requirements. Circular layouts of induction accelerators or "recirculators" have also been investigated, for the purpose of achieving a cost savings by reusing induction cores and focusing elements. Recirculators are treated in this chapter (rather than in Chap. 11) due to the expected commonality of the beam dynamics with linear accelerators, although there is also some commonality between induction synchrotrons and recirculators, as well. In all of these concepts, final peak power is achieved by compressing the beam longitudinally in a final "drift compression" section. Both linear drift sections and compressor rings have been explored conceptually.

An important choice of architecture is that between the linac and a circular machine. Because of the need to optimize the bore radius as the beam accelerates, the purely circular designs have been composed of several rings. Hybrid designs are also possible, with combinations of linac and ring. Other design questions include which focusing system (electric quadrupole, magnetic quadrupole, or solenoid) to use, whether or not to merge beams, and what number of beams to use – all of which must be answered as a function of ion energy throughout the machine. Also, the optimal charge state and mass must be chosen. These different architectures and beam parameters lead to different emittances and imply different constraints on the final focus.

Another important variable is the impact of the architecture on the development path to a fusion driver. The development path refers to the sequence of machines that would be built, ultimately leading to a fusion power plant. Some work has been done on a "modular" approach, defined here as the development of a complete accelerator (a module), which would take a beam to the final energy required for a driver, but not necessarily the final current. The IFE driver would then consist of, for example, 10–20 identical copies of the module, that together could deliver the required current on target. An advantage of the modular approach is that all the issues involving the accelerator would be resolved in developing the prototype for the single module. The development path is thus attractive in the sense that risks in achieving the accelerator goals are removed before investing in a large driver-scale system. A disadvantage of this approach, is that the cost of a modular driver is inherently larger than an optimized multiple beam accelerator. Also, the issues involving multiple beam overlap at the target are still not resolved until the final driver, so that the risk reduction is only partial.

We will describe in detail three example accelerator concepts that illustrate some of the physics and technology considerations for an IFE driver:

1. The multiple beamline, single-coreline, quadrupole-focused linac (hereafter multi-beam linac); (A coreline is defined here as the set of beamlines which thread a common set of induction cores).
2. A "modular" design, with low-energy solenoidal focusing, comprised of 20 corelines, each consisting of a single-beamline.
3. The recirculator, composed of three rings, and four beamlines and one coreline throughout.

We take the 2002 Robust Point Design as an example of the multiple-beam linac [19]. This example has 120 beams that are magnetically focused. The main reasons for having large beam numbers are three-fold: First, the large beam number maximizes the current transport through a fixed core radius, minimizing the core volume. Second, the large beam number allows a larger ratio of the required final six-dimensional phase-space volume to the initial volume out of the injector. This allows a larger increase in the transverse and parallel normalized emittances, allowing a greater safety factor in permissible emittance dilution. Third, recent LLNL target designs require a large number of beams for symmetry considerations [6, 7, 5].

In the modular approach [17, 20], the final beam energy is reduced by a factor of ten from the nominal quadrupole approach. This requires an increase in the total charge on target by the same factor. However, the reduced final energy requires much less core-material – one of the cost drivers in an induction accelerator. Also, at sufficiently low energies solenoids become more favorable for transporting charge as will be seen. Since the core material has been drastically reduced by going to lower energy, it becomes feasible to consider multiple "core-lines," which are essentially identical accelerator copies. The different scaling of transportable current of solenoids can lead to optimal designs with small numbers of beams.

Cost reduction is the main motivation for the recirculator approach, achieved through the multiple use of induction cores and quadrupoles during each acceleration sequence using the circular layout. When the required ion energy is sufficiently large, the recirculator is more compact than a multi-beam linac at the same energy. In the design of [11], the circumference ~ 2 km is dictated by the radius of curvature of a 10 GeV ion in a ~ 2 Tesla dipole magnetic field (at an average dipole occupancy of 0.33). In the linac approach the maximum accelerating gradient (of 1–2 MV/m) determines the scale of the machine (length $\sim$ 2–4 km at 4 GeV). The size of the induction cores also tends to be reduced in a recirculator, because reuse of the cores allows a smaller accelerating gradient to be used, with an associated reduction in core size.

Now let us examine the major elements of induction accelerators, emphasizing the scaling relationships of the induction cores, focusing elements, and bending elements on the variables which distinguish the three example architectures, such as number of beams, pulse duration, and accelerating gradient. Figure 10.1 shows the unit structure of a multiple beam linac, called the "half-lattice period" (hlp). Because quadrupoles focus in pairs with alternating field gradients the complete

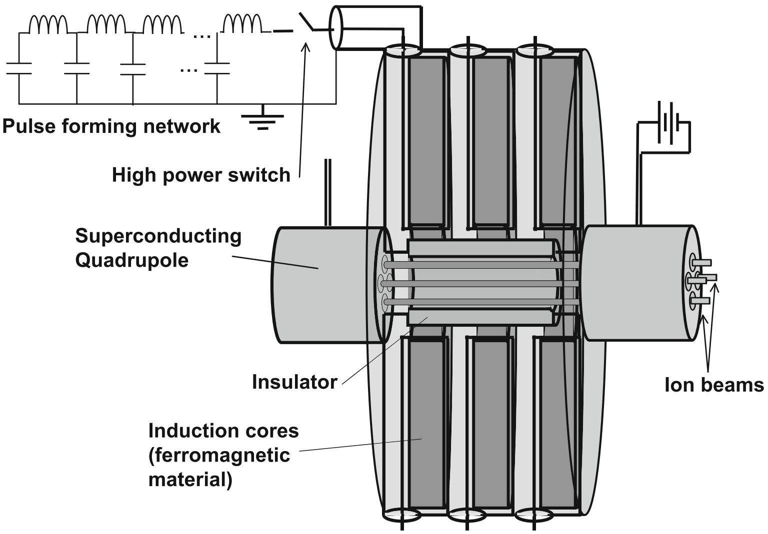

Fig. 10.1 A typical half-lattice-period of a multiple beam quadrupole linac for heavy ion fusion

lattice period consists of a pair of hlp's. The complete accelerator consists of 100's to 1,000's of hlp's. Quadrupoles are replaced by solenoids in some high current low ion energy designs, such as in some modular designs. In the recirculator a dipole bend is added to the half-lattice period. We will return to the three concepts and explicitly discuss the advantages and key issues associated with each.

10.1.4 Induction Acceleration and Energy Loss Mechanisms

Acceleration is achieved in all three concepts by the use of a series of induction modules, each module adding an energy increment to the beam. The induction cell consists of the induction core, which is an annulus of ferromagnetic material and a modulator, which consists of a set of capacitors or a pulse forming network for energy storage and a switch. The principle is the same as that of a transformer, in which the beam (which threads the core) acts like a "one-turn" secondary of the transformer (see Chap. 3). As in the case of a transformer, Faraday's law relates the voltage increment ΔV, and pulse duration Δt to the cross-sectional area of the annulus A and the change in magnetic flux ΔB (see Sect. 3.5):

$$\Delta V \Delta t = A \Delta B. \tag{10.6}$$

Since the total volume of ferromagnetic material (such as Metglas, or Ferrite) is a major cost of the accelerator, keeping either the pulse duration short or the voltage increment small is essential to having cores of reasonable areas and volumes. In the linac approaches, a high voltage gradient is desirable to minimize costs. In the recirculator approach, the cores are reused, so the voltage gradient can be reduced and/or pulse durations can be longer. In the recirculator example examined in this paper this flexibility is used to increase the pulse duration in the early part of the machine and reduce the number of beams.

The modulators in a recirculator will be different from those chosen in any of the linac approaches. In the linac examples, a voltage pulse is a applied to the core just once per "shot" so the repetition rate is the rate at which the fusion targets are shot, a few Hz. In the recirculator example the cores are fired once each lap, so repetition rates up to of order 100 kHz are required. Further, as the beam accelerates, the pulse repetition rate increases, and because of the velocity increase and bunch compression the pulse duration decreases. The modulators on a linac are envisioned as pulse forming networks of capacitors and inductors (see Chap. 4), which form a pulse of a fixed duration and fixed waveform, after being initiated by a high-power switch such as a thyratron. The recirculator designs use capacitors for energy storage, which are discharged using arrays of solid state switches (MOSFETS), to both initiate and terminate the pulse. Arrays are required because many switches are required in series to hold the required voltage, and in parallel to carry the required current. Although, arrays of solid-state switches are individually more expensive than the pulse forming network approach, the smaller number of modulators required in a recirculator permits their use, despite their higher unit cost. As costs decrease in time, it will be necessary to reevaluate whether or not solid state switches will be affordable for linacs, as the main switch for the induction cores. They already may be competitive for auxiliary tasks, such as lower power correction pulses.

For a fusion power plant to be practical, the driver must be highly efficient in converting wall plug power into beam power. Efficiencies in the range of 20–30% are calculated to be possible using induction acceleration. One of the main sources of energy loss in induction linacs is dissipative losses in the induction cores (see Sect. 5.4). "Eddy current" losses arise when inductive electric fields within the cores create currents, producing resistive losses. Again using Faraday's law, the inductive field E is proportional to geometric factors times $\partial B/\partial t \simeq \Delta B/\Delta t$. The current density J is given by $J = \sigma_c E$, where σ_c is the conductivity, so that the power lost per unit volume is proportional to $J \cdot E \sim \sigma_c E^2 \sim \Delta B^2/\Delta t^2$. Over the course of a pulse of duration Δt the energy dissipated per unit volume is thus proportional to $\sigma_c \Delta B^2/\Delta t$. This argument applies to tape wound cores (ribbons), where the eddy currents are within each layer of tape (as in Metglas).

As the pulse duration gets very long, the eddy current losses go toward zero. Hysteresis losses contribute a second form of energy loss. This is the energy required to reorient the domains of magnetic flux along the imposed field direction. As the rate of change of the flux goes to zero this loss approaches a value proportional to the total change in flux ΔB. Empirically, the losses per unit volume $\mathcal{L}$ can be expressed approximately as in Chap. 5 (cf. Eq. 5.2):

$$\mathcal{L} \simeq 750 \left(\frac{\Delta B}{2.5\ \text{Tesla}}\right)^2 \left(\frac{1\ \mu s}{\Delta t}\right) + 100 \left(\frac{\Delta B}{2.5\ \text{Tesla}}\right)\ \text{J/m}^3. \tag{10.7}$$

Here the coefficients depend on the choice of magnetic material which in this case is Metglas 2605-S2.

Consider an accelerator that has a constant acceleration gradient [16] $\mathrm{d}V/\mathrm{d}s = (V_f - V_i)/N_{\text{gap}}L$. Here subscripts i and f indicate initial and final values respectively, and N_{gap} is the number of accelerating cores encountered by the beam (which for a recirculator is equal to the number of turns times the number of half-lattice periods in the ring). As an illustration, consider a pulse duration that decreases linearly with distance (or voltage), so that

$$\Delta t = \Delta t_i + (\Delta t_f - \Delta t_i)\frac{V - V_i}{V_f - V_i}. \tag{10.8}$$

In that case, the total loss in the inductive cores $\mathcal{L}_{tot}$, under these assumptions is given by:

$$\mathcal{L}_{\text{tot}} = \left[4.7\ \text{MJ} \left(\frac{\mathrm{d}V/\mathrm{d}s}{1\ \text{MV/m}}\right)\left(\frac{0.5\ \text{m}}{R_{\text{out}} - R_{\text{in}}}\right)\left(\frac{0.8}{\eta_{\text{core}}}\right) + 0.63\ \text{MJ}\right] \times \left(\frac{R_{\text{out}} + R_{\text{in}}}{1\ \text{m}}\right)\left(\frac{V_f - V_i}{10\ \text{GV}}\right)\left(\frac{\Delta t_i + \Delta t_f}{1\ \mu\text{s}}\right) \tag{10.9}$$

Here, the core inner and outer radii are given by R_{in} and R_{out}, respectively, and η_{core} is the ratio of the core length to the distance between accelerating gaps. Note that core losses can be reduced by going to small accelerating gradients and by increasing core volume so that the cores operate away from saturation. Both effects will reduce the first term in $\mathcal{L}_{\mathrm{tot}}$, and can be carried out until hysteresis dominates the core loss. The recirculator operates at a much lower accelerating gradient and therefore will have more efficient acceleration. High-charge state machines have much lower V_f and can also have more efficient acceleration when operating at high current through each core.

In recirculators, a second major source of energy loss is present. As the energy of the beam increases during the acceleration of a beam pulse, so too must the dipole field which bends the beam. The scale over which the acceleration occurs is a few milliseconds, which is faster than the permissible ramping time of present-day superconducting magnets. Conventional magnets must be used, with losses generally proportional to the magnetic field energy (proportional the square of the field B). In the magnets under consideration for recirculators, losses arise from four major sources [21]. These are:

1. Resistive losses in the conducting wire coils (proportional to $I^2RP \sim B^2P$, where I is the current, R is the wire resistance, and P is the residence time of the beam within the ring).
2. Eddy currents within the conductors ($\sim B^2x^3/P$ where x is the width of the wire).
3. Eddy current losses in the laminated iron yokes needed to confine and direct the magnet flux (also proportional to B^2/P).
4. Hysteresis loss in the iron.

In driver recirculator designs $\sim$40 MJ of magnetic energy is stored in the magnetic field. Efficient recovery of this energy for subsequent pulses is required to achieve overall high efficiency of the accelerator. Dipole designs (including the effects of cooling channels) in which $\sim$90% of the magnetic energy is reused each pulse appear achievable.

10.1.5 Scaling of the Focusing Systems

In the absence of acceleration, the envelope equations for the three focusing systems can be expressed as:

$$\frac{\mathrm{d}^2 a_x}{\mathrm{d}s^2} = \frac{\varepsilon^2}{a_x^3} + \begin{cases} \frac{2Q}{a_x+a_y} \pm \frac{V_q}{V}\frac{a_x}{r_p^2}, & \text{Electric Quadrupole} \\ \frac{2Q}{a_x+a_y} \pm \left(\frac{qB_q^2}{2mV}\right)^{1/2}\frac{a_x}{r_p}, & \text{Magnetic Quadrupole} \\ \frac{Q}{a_x} + \frac{\omega^2 a_x}{v_z^2} - \frac{\omega\omega_c a_x}{2v_z^2}, & \text{Solenoid} \end{cases} \tag{10.10}$$

Here, a_x and a_y are the envelope radii in the x- and y-directions, $Q = \lambda/(4\pi\varepsilon_0 V)$ is the perveance, qV is the ion energy, q and m are the charge and mass of the particle, ω is the rotation frequency of the beam envelope, ω_c is the cyclotron frequency, ε is the unnormalized beam emittance, v_z is the axial beam velocity, and r_p is the clear aperture (beam-pipe) radius. For the quadrupole case, the equation for a_y is found by interchanging a_x with a_y in Eq. (10.10). For the solenoid case, the beam is axisymmetric, i.e., $a_x = a_y = a$. Also in the solenoid case, the focusing results from the difference between the outward centrifugal force due to beam rotation and the inwardly directed $v_\theta B_z$ force, where v_θ is the azimuthal beam rotation velocity and B_z is the solenoidal magnetic field. In addition, space charge and emittance tend to defocus the beam.

In the quadrupole case the beam alternately receives "kicks" which focus then defocus, but since the focusing occurs when the beam is at larger radius where the kicks are stronger, there is an average net focusing. We may average over a lattice period to obtain a smooth approximation to the focusing [22]. In the solenoid case, we may maximize the focusing by choosing $\omega = \omega_c/2$. Then, all three focusing systems may be represented approximately by an envelope equation for the average beam radius a

$$\frac{\mathrm{d}^2 a}{\mathrm{d}s^2} = \frac{\varepsilon^2}{a^3} + \frac{Q}{a} - k^2 a. \tag{10.11}$$

Here,

$$k^2 \equiv \begin{cases} \frac{1}{4r_p^2}\left(\frac{\eta L}{r_p}\right)^2\left(\frac{V_q}{V}\right)^2, & \text{Electric Quadrupole,} \\ \frac{1}{8}\left(\frac{\eta L}{r_p}\right)^2\left(\frac{qB_q^2}{mV}\right), & \text{Magnetic Quadrupole,} \\ \frac{\eta}{8}\left(\frac{qB_s^2}{mV}\right), & \text{Solenoid.} \end{cases} \tag{10.12}$$

Here, η is the fractional quadrupole or solenoid occupancy in the lattice. Note that for electrostatic quadrupoles k^2 is proportional to $1/V^2$ whereas for magnetic quadrupoles k^2 varies as $1/V$ suggesting that at low voltages electrostatic quadrupoles will be more effective than magnetic quadrupoles. Note also that for quadrupole focusing the focusing constant increases as the lattice period increases, whereas for solenoids the constant is independent of lattice period.

The particle undergoes quasi-harmonic betatron motion with wave number k. The phase advance (in the absence of space charge) σ_0 is approximately given by $\sigma_0 = 2kL$ designated per lattice period $2L$. Note that for aligned solenoids the period $2L$ contains a single magnet, but two magnets for alternating solenoids, whereas there are two quadrupoles in period $2L$.

For all three systems, the phase advance cannot be made arbitrarily large. Envelope/lattice instabilities set in for $\sigma_0 \gtrsim \pi/2$ [23–25].

By eliminating the lattice period $2L$ in favor of σ_0, and equating the space charge term Q/a to the focusing term $k^2 a$ in Eq. (10.7) (ignoring the normally small contribution from the emittance term), we may calculate the maximum transportable line charge density per beam λ_b. This is one form of the so-called "Maschke limit:"

$$\lambda_b = \begin{cases} 0.9\ \frac{\mu\mathrm{C}}{\mathrm{m}} \left(\frac{\sigma_0}{1.4}\right) \left(\frac{a/r_p}{0.7}\right)^2 \left(\frac{\eta}{0.7}\right) \left(\frac{V_q}{80\ \mathrm{kV}}\right) & \text{Electric Quad} \\ 1.0\ \frac{\mu\mathrm{C}}{\mathrm{m}} \left(\frac{\sigma_0}{1.4}\right) \left(\frac{a/r_p}{0.7}\right)^2 \left(\frac{\eta}{0.7}\right) \left(\frac{B_q}{2\ \mathrm{Tesla}}\right) \left(\frac{(q/e)/A}{1/200}\right)^{1/2} & \\ \qquad \times \left(\frac{V}{2\ \mathrm{MeV}}\right)^{1/2} \left(\frac{r_p}{6\ \mathrm{cm}}\right) & \text{Magnetic Quad} \\ 0.03\ \frac{\mu\mathrm{C}}{\mathrm{m}} \left(\frac{a/r_p}{0.7}\right)^2 \left(\frac{\eta}{0.7}\right) \left(\frac{B_s}{2\,\mathrm{Tesla}}\right)^2 \left(\frac{(q/e)/A}{1/200}\right) \left(\frac{r_p}{6\ \mathrm{cm}}\right)^2 & \text{Solenoid} \end{cases} \tag{10.13}$$

Here, A is the mass of the ion in amu. Note that the line charge density limit per beam λ_b increases with voltage V only for the magnetic quadrupoles, which leads to the choice of magnetic quadrupoles for the high energy section for two of the three example concepts described here. Note also that, although the line charge density limit for the solenoids has a smaller coefficient at the nominal values of the field and pipe radius indicated, λ_b increases with the square of $B_s r_p$, whereas for the quadrupoles it rises linearly with $B_q r_p$.

Also note that λ_b is independent of r_p for electrostatic quadrupoles, proportional to r_p for magnetic quadrupoles, and r_p^2 for solenoids. We define a second relevant quantity λ_{tot} equal to the total line charge that can be transported through an induction core of fixed inner radius R_{in}. We follow the argument of Bangerter [26], adding solenoidal focusing to the discussion.

The number of beams N_b threading each induction core is proportional to $(R_{\mathrm{in}}/r_q)^2$ where r_q is the outer radius of the quadrupole or solenoid (for large N_b) (see Fig. 10.2). Assuming that r_q/r_p is constant as one changes the number of beams, then the total transportable line charge $\lambda_{\mathrm{tot}} \sim V_q N_b$ for electric quadrupoles, $B_q N_b^{1/2}$ for magnetic quadrupoles, B_s^2 for solenoids. Further, $V_q \sim r_p^{1/2 \text{ to } 1}$ to avoid breakdown, and for small magnetic field values B_q and B_s are proportional to I_m/r_p where I_m is the total current in the magnet. But $I_m \sim J_{\mathrm{crit}} r_p^2$ where J_{crit} is the critical current density for superconducting magnets, and is assumed here to be only weakly dependent on field strength. Thus B_q and B_s are proportional to r_p for fixed ratio r_q/r_p which suggests that $\lambda_{\mathrm{tot}} \sim N_b^0$ (for magnetic quadrupoles) and $\lambda_{\mathrm{tot}} \sim N_b^{-1}$ (solenoids). For large r_p and magnetic fields, for technological and economic reasons the magnets are designed at nearly constant maximum values, so that $\lambda_{\mathrm{tot}} \sim N_b^{1/2}$ (for magnetic quadrupoles) and $\lambda_{\mathrm{tot}} \sim N_b^0$ (solenoids). Summarizing these scalings, we find:

$$\lambda_{\mathrm{tot}} \sim \begin{cases} N_b^{1/2 \text{ to } 3/4}, & \text{Electric Quadrupole} \\ N_b^{0 \text{ to } 1/2}, & \text{Magnetic Quadrupole} \\ N_b^{-1 \text{ to } 0}, & \text{Solenoids} \end{cases} \tag{10.14}$$

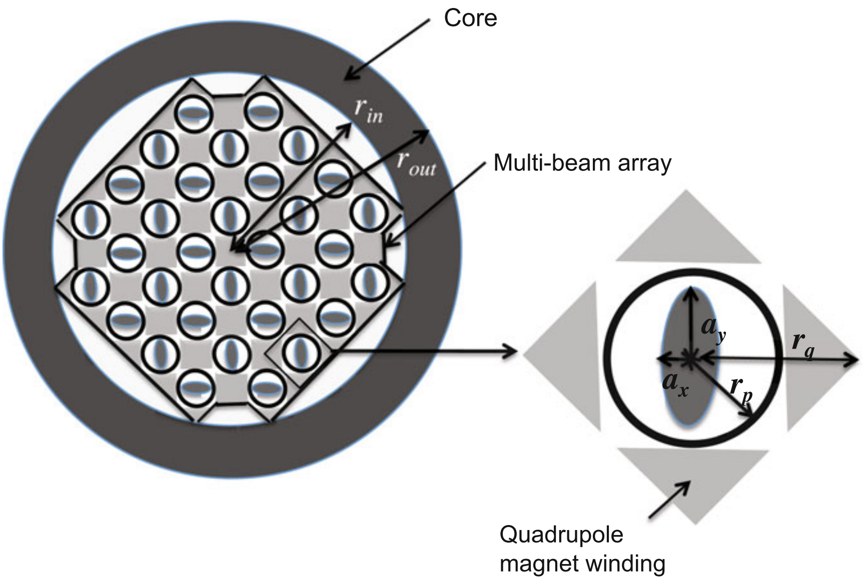

Fig. 10.2 A quadrupole array showing multiple beamlines with shared conductors threading a single induction coreline

From Eq. (10.9), it is apparent that for electrostatic quadrupoles a larger number of beams is optimal, for magnetic quadrupoles larger numbers of beamlines are somewhat favored, but for solenoids a smaller number of beamlines will be optimal. Indeed, (a/r_p) multiplies the above expression, and since finite alignment precision suggests that a/r_p tends to zero as a tends to zero (or N_b tends infinity), even for electric quadrupoles an upper limit on the number of beams for maximum transportable current is reached. It is thus apparent how the scaling of transportable current leads to a large number of beams in accelerators with electric quadrupole "front ends," and a small number of beams in an accelerator with solenoids in the low energy section.

10.1.6 Accelerator Scaling with Charge-to-Mass Ratio

In order to obtain a qualitative understanding of how accelerator costs scale with charge-to-mass ratio q/m we may consider a simplified example using quadrupole transport to illustrate the scaling. In comparing drivers which use different charge-to-mass ratios, target requirements constrain the driver to maintain the same pulse energy $Q_{\text{ctot}}V_f$, the same pulse duration at the target Δt_t, and the same ion range R. Here Q_{ctot} is the total charge in the bunch, and qV_f is the final ion energy. A crude low order approximation (but sufficient for our purposes) of the mass and energy dependence of the range R is that R depends only on β where βc is the ion velocity. (This neglects a slow decrease in range as the atomic mass increases, at fixed β).

Under these assumptions $qV_f/m \simeq$ constant. This directly implies that $V_f \sim m/q$ and $Q_{\rm ctot} \sim q/m$. For a linac the accelerator length $L_{\rm acc}$ decreases for large q/m since $L_{\rm acc} \sim V_f/({\rm d}V/{\rm d}s) \sim m/q$. Here ${\rm d}V/{\rm d}s$ is the maximum accelerating gradient, which is typically $\sim$ 1–2 MV/m for induction linacs. For larger q/m the space charge increases. For a concrete comparison, we make the additional assumption that the voltage, pulse duration, and geometry of the injector (such as r_p) are fixed, but that as q/m is altered the number of beams changes to account for the changes in required space charge. Under those assumptions,

$$\begin{aligned} N_{bi} &\sim \tfrac{Q_{\rm ctot}}{\ell_{bi}\lambda_{bi}} \sim \left(\tfrac{q}{m}\right)^{1/2}, && \text{Electric Quadrupole,} \\ N_{bf} &\sim \tfrac{Q_{\rm ctot}}{\ell_{bf}\lambda_{bf}} \sim \left(\tfrac{q}{m}\right), && \text{Magnetic Quadrupole.} \end{aligned} \tag{10.15}$$

Above $Q_{\rm ctot} \sim q/m$ (for both electric and magnetic quadrupoles), $\ell_{bi} \sim (q/m)^{1/2}$ and $\lambda_{bi} \sim 1$ (for electric quadrupoles), while $\ell_{bf} \sim 1$ and $\lambda_{bf} \sim 1$ (for magnetic quadrupoles), and where subscripts i and f represent initial and final, respectively.

We again assume for this example that the pulse duration decreases linearly with distance [see Eq. (10.8)]. The required total volt-second capability of the accelerator is given by $\int \Delta t({\rm d}V/{\rm d}s){\rm d}s = \int \Delta t{\rm d}V \sim m/q$. Hence the inner radius of core $\sim N_b^{1/2} \sim (q/m)^{1/2 \text{ to } 1/4}$, and the total core volume and core costs $\sim (m/q)^{1/2 \text{ to } 3/4}$. This result suggests that there can be a cost savings associated with larger q/m. As will be discussed in the next section, the challenges for this approach arise from more stringent requirements at the final focus and at the injector.

10.1.7 Multi-Beam Linac with Quadrupole Focusing

The multi-beam linac has undergone the most research over the last 20 years. See Fig. 10.3 for a schematic of the various elements and beam manipulations in a multiple-beam linac approach to heavy ion fusion. Systems codes have been developed which [27] to put each of the various accelerator configurations onto a common cost and efficiency basis. The codes have been applied to accelerator designs that have been specifically tailored to recent LLNL target designs [8]. One design, hereafter called the Robust Point Design or RPD [19] consisted of 120 beams of singly charged Bismuth (injected with a pulse energy of 1.6 MeV and pulse duration of 30 µs.) Since the target required a prepulse at lower energy (3.3 GeV), once this prepulse energy is reached, 48 of the beamlines are transported outside the main induction cores while the remaining 72 beams continue acceleration to 4 GeV. The main pulse exits the accelerator at 200 ns and undergoes drift compression, reaching approximately 9 ns at the target. (The prepulse is similarly compressed from 200 to approximately 38 ns). The pulse shape is built up from five different "rectangular" pulses having varying pulse width and phase, but add to a desired pulse shape determined by target physics. Another design [27] consisted of 192 beams transported with electrostatic quadrupoles to 100 MeV after which the beams merged

Fig. 10.3 The multiple beam linac approach to heavy ion fusion, with various beam manipulations indicated

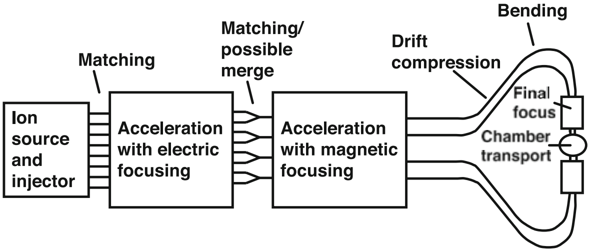

into 48 beams transported by magnetic quadrupoles. In addition to the beneficial transport properties of electric quadrupoles at low energy, they also tend to clear electrons out of the beam, which is most critical at low energy. At low energy, the pulse duration is long so the beam is most vulnerable to electron accumulation, since the longer time allows ionized residual gas particles time to reach the walls liberating electrons and ions, and thus possibly causing emittance dilution to the latter part of the beam.

Although heavy ion fusion relies on technology that has been validated on other accelerators, including induction accelerators, the ion beam intensity required for heavy ion fusion has not been achieved on any existing machine. For the multibeam linac concept some of the key physics and technology issues, that would require validation in a HIF research program (see e.g. [28]) include:

1. Control and alignment of multiple-beam arrays. Since there have been few experiments with such large arrays of ion beams, there have been few attempts to quantify the requirements on the alignment and control system.
2. Transport of beams with large head-to-tail velocity tilt. This is an issue which affects all of the accelerator concepts and ultimately becomes a question of what velocity tilt can be transported without inducing mismatch oscillations on the beam.
3. Inter-beam interactions in gaps. In a high gradient machine the acceleration gaps are either longer or are graded, making this issue more important for this concept. Methods for shielding the beams within the gaps need to be assessed.
4. Emittance dilution from merging. The question of whether or not to merge is ultimately an issue of system optimization (some designs have, in fact, no merging), since the emittance dilution associated with a beam merge must be accounted for in an optimized design. Simulations and recent experiments [29] will help resolve this issue.
5. Electron-cloud effect. During magnetic quadrupole or solenoid transport electrons (originating from the walls, created by ion or secondary impacts, or from collisions with the residual gas) can accumulate in long pulses and if sufficiently dense degrade beam quality [30, 31].
6. Cost. The driver cost must be evaluated carefully for this concept as well as any concept for HIF.

Fig. 10.4 The MBE-4 induction accelerator that demonstrated acceleration and compression of four beams in an electrostatically focused accelerator

A multi-beam linac (MBE-4) with four beams was constructed at LBL in 1982. It provided a proof of principle for simultaneous acceleration and compression of four beams in an induction linac to 2 MeV [32]. See Fig. 10.4.

10.1.8 Modular Drivers

As discussed earlier, a key question is how to create a sequence of accelerators which allow key concept validations without risking large capital investments. In an effort to solve that problem, the "modular" approach whereby, a complete subset or "module" of an HIF driver can be created and tested at a fraction of the cost ($\sim$5–10%) of a complete driver. The driver then consists of tens to hundreds of identical copies of each module, all focused onto the target. Examples of modular designs are given in Yu et al. [20] and Logan [33]. One approach to accomplish this task is based on a linac that is solenoidally focused, and has a final energy of only a few 100 MeV instead of a few GeV. Figure 10.5 shows one module of a concept that accelerates stripped Rubidium, charge state +9, through 100 MV (with a resulting ion energy of 900 MeV). As in the multi-beam linac, there are several manipulations required to reach the intensities required for HIF. In Fig. 10.6 each

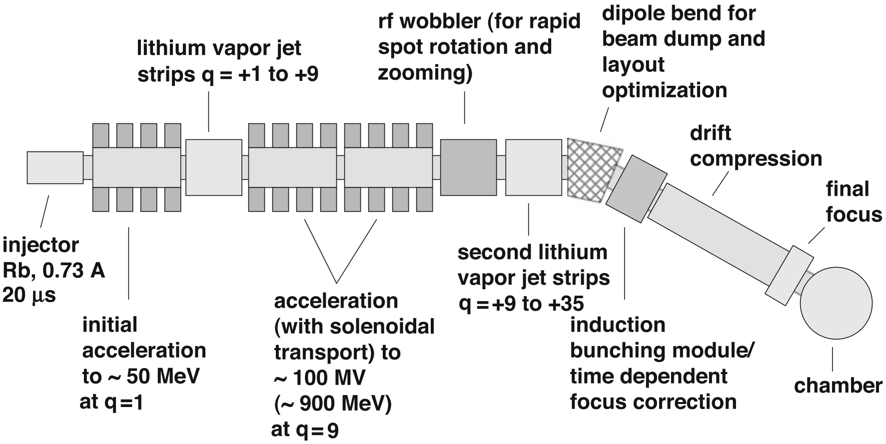

Fig. 10.5 A typical accelerator "module" in the modular, solenoid based, multiple linac approach to heavy ion fusion [33]

accelerator module lies on one of two cylindrical surfaces, and the drift sections lie on cones with polar opening angles of 10° and 55°.

There are a number of key issues associated with this concept. The accelerator requires a large current ion source. No experience with such sources has as of yet been obtained. A second major concern is aberrations from the fringe fields of laterally adjacent solenoids. Multiple beam arrays are not as naturally compatible as they are with quadrupoles. With solenoids, the flux through the end of one solenoid interacts in a non-axisymmetric manner with the flux from an adjacent one, producing large non-linear field aberrations, unless the flux from the solenoids is contained or they are separated a sufficient distance. A third issue is the control of backflowing electrons flowing down magnetic field lines and achieving high energy going through multiple gaps. Alternating the field direction longitudinally in adjacent solenoids has been suggested, but flux lines which terminate on the walls may be a source for electrons and thus may do more harm than good.

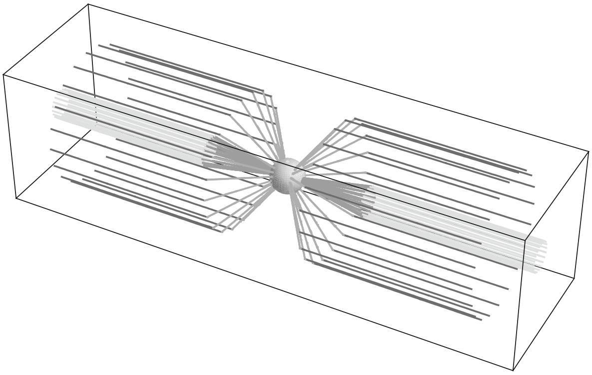

Fig. 10.6 The layout of the modular, multiple-linac approach of [33]. Each module is ∼ 100 m in length (see Fig. 10.5)

10.1.9 Recirculator

The recirculator as envisioned in [11] consisted of several rings, each increasing the energy by a factor of about 10 and decreasing the pulse duration by a factor of about three. See Fig. 10.7. The prime motivation for the study was to see if it was possible to substantially reduce the cost of the accelerator relative to a linac design. Further, the authors tried to design a machine with a small number of beams, favoring the simplicity of four beams relative to the complexity of the large number of beams in the linac approach, and eliminating the need to merge beams with the associated emittance growth. Designing a machine with fewer beams, however, meant the design relied on large initial pulse durations in order to satisfy the constraint of Eq. (10.4). Since the recirculator can operate at a reduced acceleration gradient (because the accelerator components are reused over the course of ~ 100 turns), long pulse durations can be entertained more easily in a recirculator than in a linac, without requiring very large induction cores [see Eq. (10.6)].

However, because of the smaller accelerating gradient, the beam covers a much larger path length. Beam loss from residual gas and charge-changing collisions of beam particles with each other are more problematic in a recirculator, and the poorly understood effects of lost beam and ionized residual gas hitting the wall, producing additional outgassing (a beam intensity dependent effect) needs experimental verification to establish that the vacuum behaves as predicted. As indicated above, the efficiency of ramped dipoles is crucial to the recirculator design, since the recycled dipole energy is larger than the beam energy itself. Insertion/extraction of multiple beams into and out of the ring also requires validation. In one recirculator design study [11] the beam lines were arrayed in a square pattern within the bend sections (to minimize core volume), but were arrayed vertically in the insertion/extraction section to facilitate use of the rectangular quadrupoles used for getting the beam into and out of the ring. This arrangement allowed path equalization by exchanging inner

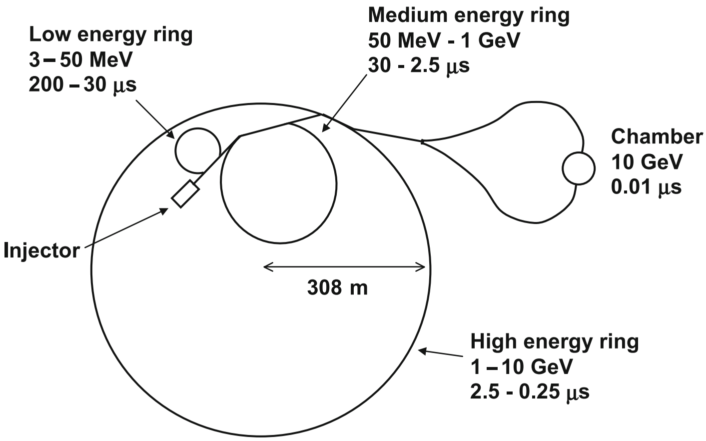

Fig. 10.7 The layout of the recirculator from [11]

beams with outer beams in the bends. Use of superconducting quadrupoles provides an efficient focusing system and constant magnetic field. As the beam accelerates, the tune changes rapidly, effectively passing through resonances. As a result, the recirculator operates in a space-charge-dominated regime, far exceeding the Laslett tune shift limit of conventional circular accelerators. Validation of this operation point experimentally is a key goal of the bending and recirculation experiments that took place at LLNL [34, 35] and are taking place at the University of Maryland [36, 37]. Finally, the long pulse durations which enabled a small number of beams to be accelerated at the beginning of the accelerator, imply larger momentum spread at the end of the accelerator, and there is less leeway for phase space dilution. Injectors with smaller voltage errors or achromatic final focusing systems would be beneficial to recirculators with long initial pulse duration. Also, recirculators with more beams and shorter pulses (hence closer in concept to "circular" linacs) need evaluation.

10.1.10 Beam Manipulations

There are number of non-standard techniques that are envisioned for induction-accelerator-based HIF. As indicated above one of these techniques increases the current and hence peak power by increasing the velocity of the tail of the beam relative to the head, thus compressing the beam longitudinally. This is one benefit from using non-relativistic beams where velocities are significantly different than the speed of light, so that a relatively small fractional change in energy $\Delta E/E$ results in a significant fractional change in velocity ($\Delta v/v \sim \Delta E/2E$) instead of ($\Delta v/v \sim (1/\gamma_r^2)\Delta E/E$) for an ultra-relativistic beam, where γ_r is the relativistic factor [$\gamma_r = (1 - v^2/c^2)^{1/2}$]. As was shown in Chap. 9, the decreasing line charge density at the beam ends creates an electric field which tends to cause the beam to expand longitudinally. For a beam which decreases monotonically from the center (as for example a beam that has a parabolic line charge density with longitudinal coordinate z) there is an outward longitudinal force over the entire beam length (except the beam center). From the earliest concepts for HIF, it was realized that this space charge force would act to remove a velocity tilt that is imposed on the beam, and under some circumstances could remove the tilt, just as the beam was passing through the final focus magnets. By coinciding this "stagnation" point with the location of the center of the final focus magnet system, minimal chromatic aberrations would result, limited only by intrinsic thermal spread of the compressed beam and any residual velocity tilt not removed by the stagnation.

We may make estimates of the magnitude of the velocity tilt needed and the length of the drift section by appealing to the longitudinal envelope equation:

$$\frac{\mathrm{d}^2\ell_b}{\mathrm{d}s^2} = \frac{\varepsilon_z^2}{\ell_b^3} + \frac{12gqQ_c}{4\pi\epsilon_0 mv^2\ell_b^2} - K(s)\ell_b. \tag{10.16}$$

Here, ℓ_b is the length of a beam with a parabolic density profile, g is the "g-factor" (cf. Eq. (9.28)), Q_c is the total charge in the beam, $K(s)$ is a possible linear longitudinal focusing field (which we assume to be zero in the drift section), and ε_z is the longitudinal emittance. For non-neutralized drift compression, the longitudinal emittance may be ignored, since the intense space charge will generally cause stagnation before the emittance term has effect. (For neutralized drift compression, the longitudinal emittance limits the ultimate minimum pulse duration). Setting $K(s) = \varepsilon_z = 0$, and integrating Eq. (10.16) once we obtain:

$$\frac{1}{2}\left(\frac{\mathrm{d}\ell_b}{\mathrm{d}s}\right)^2 + \frac{12gqQ_c}{4\pi\epsilon_0 m v^2 \ell_b} = \frac{1}{2}\left(\frac{\mathrm{d}\ell_{b0}}{\mathrm{d}s}\right)^2 + \frac{12gqQ_c}{4\pi\epsilon_0 m v^2 \ell_{b0}} \tag{10.17}$$

Noting that at the longitudinal focus $\mathrm{d}\ell_b/\mathrm{d}s = 0$, and $\mathrm{d}\ell_{b0}/\mathrm{d}s = \Delta v/v$, where Δv is the difference between the velocity of the tail of the beam and the head, we may calculate the required velocity tilt $\Delta v/v$:

$$\frac{\Delta v}{v} = \sqrt{\frac{24gqQ_c}{4\pi\epsilon_0 m v^2 \ell_{bf}}\left(1 - \frac{\ell_{bf}}{\ell_{b0}}\right)} \tag{10.18}$$

Here, ℓ_{b0} and ℓ_{bf} are the bunch length at the beginning of the drift length, and at the focus respectively. The drift length can be estimated noting that the length of the beam is reduced to its final length during the time it takes to transit the drift length:

$$l_{\text{drift}} \simeq \frac{(\ell_{b0} - \ell_{bf})}{\Delta v/v} \tag{10.19}$$

In some designs with large line charge densities, the idea of neutralized drift compression in which a plasma is injected along the propagation path has also been advanced. In this case, the neutralizing plasma eliminates the chance of vacuum breakdown, and eases the requirements on longitudinal compression. In this case, the minimum pulse duration occurs when longitudinal emittance limits further bunch compression. In contrast to unneutralized drift compression, in neutralized drift compression the final velocity spread will be that spread by the tilt imposed to compress the beam (since space charge is no longer acting to remove the tilt). In that case, however, it has been suggested that time dependent chromatic corrections be used to minimize chromatic aberrations. The time dependent chromatic corrections would occur at a position upstream of the final focus at a point where the beam has sufficiently long pulse duration (∼100 ns) so that time dependent quadupolar magnetic or electric field temporal ramps may be imposed, at reasonable power levels. The correctors must be sufficiently close to the final focus so that accumulated phase advance differences do not put unreasonable requirements on the precision of the correctors.

Other possible beam manipulations include beam merging [29] and beam splitting [38]. The former has been considered as a way to compensate for the different scaling of focusing of electric and magnetic quadrupoles. (Electric quadrupole transport is generally optimum at a smaller bore radius than magnetic quads.)

As of this writing, the National Ignition Facility is poised to achieve the first ignition of inertial confinement fusion targets, using a laser as the driver. If it is successful, the uncertainty about whether targets can ignite will be eliminated, and a major step toward the realization of inertial fusion energy will have been achieved. The focus will then shift to the best driver (and best chamber options) for inertial fusion energy. As discussed in this chapter, there appear to be several attractive options for heavy ion accelerators to fill the role of the driver. At the same time, we have outlined the areas where further research is needed to push the accelerator frontier into an unprecedented regime of ion beam power and intensity. But this regime is an area where induction accelerators could play a natural role.

10.2 Other Applications of Ion Induction Accelerators

10.2.1 High Energy Density Physics and Warm Dense Matter Physics

Although accelerators driving HIF targets to temperatures of $\sim$200 eV may be a decade or more in the future, accelerators that could drive targets to a few eV may be much closer at hand. The field of High Energy Density Physics seeks to explore the properties of matter with energy densities greater than about 10^{11} J/m^3 which corresponds to temperatures greater than 1 eV at solid density [39, 40]. Also, a regime at lower temperatures [the Warm Dense Matter (WDM) regime], with temperatures greater than about 0.1 eV, and densities at 1–100% of solid density is of interest to a variety of scientists. Induction accelerators are also well suited to investigate these regimes, because large pulse energies are required to heat matter to this temperature, and the heating must be done rapidly to avoid hydrodynamic and other means of cooling the matter.

The WDM regime is particularly interesting because it is at the cross-roads of strongly- and weakly-coupled plasmas (where ion kinetic energies can be of order the Coulomb potential energy between neighboring ions), and is at the border of degenerate and classical electron behavior (where the electron Fermi energy can be of order of the electron thermal energy). This crossroads where small parameters are no longer small, is a challenge for theorists, and confrontation of experiment with theory is essential to understand the behavior of matter at these temperatures and densities. Further, the regime can include exotic plasmas that have had little study. An example of such a plasma is pure ion plasma consisting of positively and negatively charged ions (such as bromine) with many fewer electrons than ions. Such a plasma may have similarities to electron-positron plasmas, since the species masses are essentially equal, and may also have electrical properties analogous to semi-conductors. Also of interest, is the boundary of the liquid-vapor regions in the density-temperature phase plane of many materials [41]. The precise location of the "critical point" (indicating the density and maximum temperature of the two phase region) is not known for many metals. Also, the interior of the gaseous planets and low mass stars falls squarely within the regime of WDM [39]. Spacecraft have given planetary scientists exquisitely precise measurements of the gravitational moments of the planets Jupiter and Saturn, and the equation of state becomes one of the central uncertainties in matching the calculated gravitational moments from planetary models to the observed moments from spacecraft trajectories [42]. Finally, the hydrodynamics of plasmas heated by ions, may be of interest in its own right. Instabilities can be significantly modified by the energy deposition process itself.

For quantitative WDM and HEDP experiments with heavy ions it is desirable to heat the sample as uniformly as possible. One would also like to utilize the ion beam pulse energy as efficiently as possible. Both of these objectives are fulfilled by operating near the Bragg peak (see Fig. 10.8). With a helium ion beam, for example, the required voltage is about 1 MeV, while with Ne^{+1} or Na^{+1} it is about 20 MeV. To heat an Al foil to 1 eV, the number of Ne ions required in a sub nanosecond pulse that is focused to $\sim$1 mm radius is about 2×10^{11}, or a pulse energy of about 1 J. These requirements are extremely modest compared to those of a heavy ion driver for inertial fusion. (More conventional accelerators are also being used to explore the WDM regime, but at a much higher ion energy (far above the Bragg peak) at larger range, but less efficient use of ion energy (cf. e.g: [43])).

Taken as a whole, a facility for using heavy ion beams to heat matter to Warm Dense Matter conditions will have unique characteristics (relative to lasers, pulsed-power experiments, diamond anvil, or gas gun experiments) that will allow scientific exploration of this regime. Among these characteristics are: precise control of energy deposition (a result of highly diagnosable and controllable ion current and ion energy, characteristic of accelerator-based heating); uniformity of energy

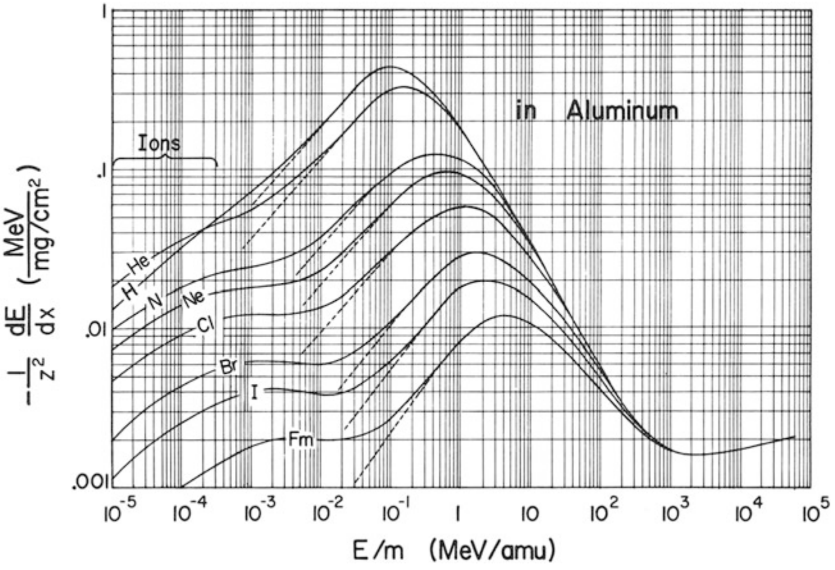

Fig. 10.8 Ion stopping rate in Aluminum as a function of energy, and ion mass (from [45])

deposition (a result of isochoric heating characteristic of ion deposition at the Bragg peak); large sample sizes compared to diagnostic resolution volumes (a result of a broad choice of ion masses and ion energies, allowing range optimization); a variety of potential targets (e.g. both conductors and insulators may be heated by ion beams); relatively long times to achieve equilibrium conditions (concomitant with the large sample sizes); a benign environment for diagnostics (low debris and radiation background, owing to the relatively low ion energy of order a few MeV/amu); high shot rates (10 per hour to 1 per second easily achievable with accelerator technology); multiple beamlines/target chambers (possible due to beam switching); sites with easy access for broad participation by university scientists and students.

By consideration of ion beam phase-space constraints, both at the injector, and at the final focus, and consideration of simple equations of state and relations for ion stopping, approximate conditions at the target foil may be calculated [44]. Thus, target temperature and pressure may be calculated as a function of ion mass, ion energy, pulse duration, velocity tilt, and other accelerator parameters. We connect some of these basic parameters to help illustrate the requirements on an ion induction accelerator for the investigation of WDM.

We first examine ion stopping, or $\mathrm{d}E/\mathrm{d}X$, where E is the ion energy and $X \equiv \int \rho \mathrm{d}z$ is the integrated range of the ion (see [45]). For heating solid aluminum (at room temperature) over a range of ion mass from 4 amu (helium) to 126 amu (iodine), the energy loss at the peak of the $\mathrm{d}E/\mathrm{d}X$ curve ($\mathrm{d}E/\mathrm{d}X|_{\max}$) may be parameterized approximately as

$$\frac{1}{Z^2}\,\frac{\mathrm{d}E}{\mathrm{d}X}\bigg|_{\max} \simeq 1.09\,\frac{\mathrm{MeV cm^2}}{\mathrm{mg}} A^{-0.82}, \tag{10.20}$$

where Z and A are the ion nuclear charge and atomic mass, respectively. Expressing $\mathrm{d}E/\mathrm{d}X|_{\max}$ as a function of A yields

$$\frac{\mathrm{d}E}{\mathrm{d}X}\bigg|_{\max} \simeq 0.35\,\frac{\mathrm{MeV cm^2}}{\mathrm{mg}} A^{1.07}. \tag{10.21}$$

Thus, the peak energy loss rate increases (nearly linearly) with ion atomic mass. Similarly, the ion energy E at the peak increases with ion mass nearly quadratically with A according to

$$E_{\max} \simeq 0.052\,\mathrm{MeV} A^{1.803}, \tag{10.22}$$

where $E_{\max}$ is E at $\mathrm{d}E/\mathrm{d}X|_{\max}$.

Target temperature uniformity is another important consideration. It has been pointed out [46] that target temperature uniformity can be maximized in simple planar targets if the particle energy reaches the maximum in the energy loss rate $\mathrm{d}E/\mathrm{d}X$ when the particle has reached the center of the foil. For any specified fractional deviation in target temperature (assuming the energy is deposited in a time short so that no hydrodynamic, radiative, or other cooling has occurred) one can determine the energy at which the ion must enter and exit the foil. From the curves of $\mathrm{d}E/\mathrm{d}X$ [45] we find that for the entrance energy to have less than a 5% lower energy loss rate relative to the peak in $\mathrm{d}E/\mathrm{d}X$, $\Delta E/E \lesssim 1.0$, where ΔE is the difference in ion energy between entering and exiting the foil, and E is the energy at which $\mathrm{d}E/\mathrm{d}X$ is maximum. The spatial width of the foil Δz, for a 5% temperature non-uniformity is then given by:

$$\Delta z = \frac{\Delta E}{\rho \left.\frac{\mathrm{d}E}{\mathrm{d}X}\right|_{\max}} \simeq 0.77\ \mu\ A^{0.733}\left(\frac{\rho_{\mathrm{al}}}{\rho}\right) \tag{10.23}$$

Here, we used $\rho_{\mathrm{al}} = 2.7$ g/cm^3 to convert the range into a physical distance. So by using materials of low density such as metallic foams, for example, the width of the foil can be relatively large, which allows longer heating times and accesses interesting densities.

The sound speed c_s is given by $c_s = (\gamma P/\rho)^{1/2} = (\gamma[\gamma - 1]U/\rho)^{1/2}$. Here, γ is the thermodynamic parameter equal to the ratio of specific heats. For an instantaneously heated target a rarefaction wave propagates inward at about c_s while matter flows outward at about $3c_s$ (for a monatomic gas) [47]. Thus, for measurement of material properties, heating needs to occur on a time scale such that the rarefaction wave does not progress so far as to render the full density region of the foil smaller than some minimum diagnosable spatial scale over the duration of the pulse.

In order to calculate more accurately the sound speed and the temperature achieved in the heating, one needs to understand the relation between energy density and target temperature. For a perfect ionized gas, the energy density is $(3/2)(1 + Z^*)(nkT)$ where Z^* is the ionization state, and n is the number density of atoms plus ions. However for solids, interaction energy of the atoms in the solid must be included, and typically for WDM the ionization state is low. For solids, the energy density is often well approximated by $3nkT$. As a first estimate, we assume $3nkT$ since we are normally interested in material with $Z^* \sim 1$. We may compare with models developed by Zeldovich and Raizer and summarized [48] or by using the Thomas Fermi model for calculating the distribution of electrons within an atom (see [49] and references therein for a description).

Using the scaling described above for ion beam stopping, the time scale for hydrodynamic expansion, and the equation of state, we are able to make estimates of the required beam parameters for exploring the Warm Dense Matter regime. Table 10.1 gives examples of requirements for Ne^{+1} ($A = 20.17$) at foil entrance energy (E_{incident}) of 19 MeV, The energy at the center of the foil (E_{center}) and the energy at the exit of the foil (E_{exit}) are listed in the caption to the table. Three different mass densities of Aluminum target are given: Solid density (2.7 g/cm^3) and 10 and 1% of solid, which can be produced by making an aluminum "foam." In turn for each target density, three target temperatures are shown. The table is based on a minimum diagnosable length scale Δz_{min} of 40 μ. It is clear from the table that solid density, although resulting in the highest energy density, requires very short pulse durations, because the foil width is smaller than Δz_{min} and only a

Table 10.1 Target parameters for a Neon beam ($Z = 10$, $A = 20.18$, $E_{\text{incident}} = 20.1$ MeV, $E_{\text{center}} = 12.1$ MeV, $E_{\text{exit}} = 7.7$ MeV, and $\Delta z_{\text{min}} = 40$ μ (from [50])

ρ (g/cm^3)(% solid)	0.027 (1%)			0.27 (10%)			2.7 (100%)		
Foil thickness (μ)	480			48			4.8		
kT (eV)	3.1	4.8	15	4.2	7.3	18	5.9	12	22
Z^*	1.1	2.1	2.7	0.56	1.7	2.6	0.56	1.2	2.5
$\Gamma_{ii} = Z^2 e^2 n_i^{1/3}/kT$	0.45	1.1	0.95	0.30	0.63	1.4	0.30	0.70	1.6
$N_{\text{ions}}/(r_{\text{spot}})^2/10^{12}$	1	3	10	1	3	10	1	3	10
Δt ns	84	48	27	3.8	2.2	1.2	0.04	0.03	0.014
U(J/m^3)/10^{11}	0.15	0.045	0.15	0.15	0.45	1.5	1.5	4.5	15

small rarefaction wave propagation distance is allowed. But for the 1 and 10% cases, the foil is larger than Δz_{min}, so that the rarefaction wave propagation distance can be 10's or 100's of microns, with concomitantly longer pulse duration. In all cases the plasma temperature is in the few to tens of eV, and the required number of particles is in the order of 10^{12}–10^{13} particles, for equivalent focal spot radii of 1 mm.

We may make simple estimates for the contribution to the spot size from chromatic effects (i.e. for the effects of a velocity spread) from particular optical systems, under the assumption that a beam plasma neutralizes both a drift compression region and the final focus. Here we choose a "thick" solenoidal lens in which a beam enters a solenoid with zero convergence angle and focuses to a spot within the solenoid. The focused beam can be shown to have a radius from emittance and chromatic effects r_{spot} given approximately by:

$$r_{\text{spot}}^2 \simeq \left(\frac{\pi r_0}{2}\right)^2 \left(\frac{\Delta v_{\text{spread}}}{v}\right)^2 + \left(\frac{2\varepsilon_x f}{\pi r_0}\right)^2 \tag{10.24}$$

Here, f is the focal length, i.e., the distance from the entrance of the solenoid to the focal spot, and ε_x is the beam emittance. Also, r_{spot} and r_0 are the beam radii ($= 2^{1/2}\langle r^2\rangle^{1/2}$) at the focal spot and entrance to the solenoid respectively, and $\varepsilon_x = 4(\langle x^2\rangle\langle x'^2\rangle - \langle xx'\rangle^2)^{1/2})$ is the unnormalized emittance. The quantity r_{spot} is minimum when $r_0^2 = (2/\pi)\varepsilon_x f/(\Delta v_{\text{spread}}/v)$ and has the value given by

$$r_{\text{spot}}^2 = 2\varepsilon_x f \frac{\Delta v_{\text{spread}}}{v}. \tag{10.25}$$

Simulations [51, 52] and analysis [44] shows that the beam intensity is not uniformly distributed over the spot radius, but is peaked resulting in somewhat higher central intensities than would be inferred from Eq. (10.25). Other effects such as the defocusing effect from the induction buncher, and the physics of beam neutralization are considered in [53].

At minimum pulse duration a velocity "tilt" becomes a velocity spread, so achieving high beam intensity will limit the velocity tilt.

It is apparent from Eq. (10.25) that a large velocity spread has deleterious effects in the focusing. Thus a larger velocity tilt will allow a shorter pulse but will yield a large overall spot. If the longitudinal emittance is small a larger velocity tilt is not needed to achieve the short pulse duration. Thus to obtain a small spot there are tradeoffs that can be made between longitudinal and transverse emittance; a different optimization might be made if one is easier to minimize than the other. This may be made more explicit by expressing Eq. (10.25) in terms of the transverse and longitudinal normalized emittances:

$$r_{\text{spot}}^2 = \frac{4\varepsilon_{nx}\varepsilon_{nz} f}{3^{1/2}\beta^3 c\Delta t} \tag{10.26}$$

Here, ε_{nx} is the normalized x-emittance ($= \beta\varepsilon_x$) and ε_{nz} is the normalized z (longitudinal) emittance (defined here as $= 3\beta(\langle z^2\rangle\langle z'^2\rangle - \langle zz'\rangle^2)^{1/2}$), f is the final focal length, β is the final velocity in units of c and Δt is the final pulse duration. A prime indicates derivative with respect to path length.

We may use the ion stopping equations, together with injector and final focus equations to examine the overall target performance as a function of ion energy, mass and other parameters. At the injector end, the normalized emittance may (ideally) be related to the temperature T_s and radius r_b of the source (cf. Eq. (9.9)):

$$\begin{aligned}\varepsilon_{nx} &= 2r_b\left(\frac{kT_s}{mc^2}\right)^{1/2}\\ &= 0.81\text{ mm-mrad}\left(\frac{r_b}{4\text{ cm}}\right)\left(\frac{20.1}{A}\right)^{1/2}\left(\frac{kT_s}{2\text{ eV}}\right)^{1/2}\end{aligned} \tag{10.27}$$

Even if the injector emittance is dominated by optical aberrations an effective temperature may be used in Eq. (10.27). To avoid voltage breakdown, the diode gap distance d must be sufficiently large (cf. Eq. (9.7)):

$$d = 0.01\text{ m}\left(\frac{V_d}{100\text{ kV}}\right)^2 \quad \text{if } d > 1\text{ cm} \tag{10.28}$$

Since we are considering large currents, $d > 1$ cm is appropriate, we may combine Eqs. (10.27) and (10.28) to obtain an equation for the final emittance

$$\varepsilon_f = 29\text{ mm-mrad}\left(\frac{4}{\Delta}\right)\left(\frac{kT_s}{2\text{ eV}}\right)\left(\frac{V_d}{400\text{ kV}}\right)^2\left(\frac{20\text{ MeV}}{qV_f}\right)^{1/2}. \tag{10.29}$$

The Child-Langmuir current is (cf. Eq. (9.15))

$$\begin{aligned}I &= \left(\frac{4\pi\epsilon_0}{9}\right)\left(\frac{2q}{m}\right)^{1/2}\left(\frac{V_d^{3/2}}{\Delta^2}\right)\\ &= 0.6\text{ }A\left(\frac{20}{A/q}\right)^{1/2}\left(\frac{4}{\Delta}\right)^2\left(\frac{V_d}{400\text{ kV}}\right)^{3/2}.\end{aligned} \tag{10.30}$$

Here $\Delta = d/r_b$ which is usually in the range 2.5–8 to minimize nonlinearities. Here we choose 4 as a typical nominal value. The total charge $I\Delta t$ is

$$I\Delta t = 0.12\ \mu\text{C}\left(\frac{20}{A/q}\right)^{1/2}\left(\frac{4}{\Delta}\right)^{2}\left(\frac{V_d}{400\ \text{kV}}\right)^{3/2}\left(\frac{\Delta t_d}{200\ \text{ns}}\right), \tag{10.31}$$

and the final pulse energy E_{pulse} is

$$\begin{aligned} E_{\text{pulse}} = V_f I\Delta t = 2.4\ \text{J}\left(\frac{20}{A/q}\right)^{1/2}\left(\frac{4}{\Delta}\right)^{2}\left(\frac{V_d}{400\ \text{kV}}\right)^{3/2} \\ \times\left(\frac{\Delta t_d}{200\ \text{ns}}\right)\left(\frac{V_f}{20\ \text{MV}}\right). \end{aligned} \tag{10.32}$$

Equations (10.27), (10.28), (10.29), (10.30), and (10.31) describe the phase space and total charge obtainable from an injector. The final target energy density U can be calculated from the total pulse energy, spot radius, foil thickness,

$$U = \frac{2V_f I\Delta t}{3\pi r_{\text{spot}}^2 \Delta z} \tag{10.33}$$

and the target temperature can be expressed as:

$$\begin{aligned} kT_{\text{targ}} &\simeq \frac{2UA_{\text{targ}}m_{\text{amu}}}{3(Z^*+1)\rho} \\ &= 3\ \text{eV}\left(\frac{A_{\text{targ}}}{27}\right)\left(\frac{3}{Z^*+1}\right)\left(\frac{2\ \text{eV}}{kT_s}\right)^{1/2}\left(\frac{0.05}{\Delta v/v_{\text{tilt}}}\right)\left(\frac{q}{1}\right)^{0.32} \\ &\left(\frac{4}{\Delta}\right)\times\left(\frac{\Delta t_d}{200\ \text{ns}}\right)\left(\frac{V_d}{400\ \text{kV}}\right)^{-1/2}\left(\frac{V_f}{20\ \text{MV}}\right)^{0.815}\left(\frac{0.7\ \text{m}}{f}\right). \end{aligned} \tag{10.34}$$

Here m_{amu} is mass of an atomic mass unit. As discussed before, the target temperature in Eq. (10.34) can be achieved if the pulse duration is sufficiently small compared to the hydro time. The pulse duration at the target Δt_t can be expressed as

$$\begin{aligned} \Delta t_t &= \frac{2\varepsilon_{nz}Am_{\text{amu}}c}{qV_f\Delta v/v_{\text{tilt}}} \\ &= 1\ \text{ns}\left(\frac{\varepsilon_{nz}}{8\ \text{mm-mrad}}\right)\left(\frac{20\ \text{MeV}}{V_f}\right)\left(\frac{A/q}{20}\right)\left(\frac{0.05}{\Delta v/v_{\text{tilt}}}\right), \end{aligned} \tag{10.35}$$

where $\Delta v/v_{\text{tilt}}$ is the head-to-tail tilt imposed on the beam during final drift compression.

These equations give estimates of the requirements for an induction linac (or any pulsed ion beam driver) using Bragg peak heating, neutralized drift compression and final solenoidal focus for the purpose of investigating Warm Dense Matter. Other concepts which choose different technological assumptions (for example, the use of time-dependent focusing) can change the requirements on the beam.

Experiments [54] using the technique of compressing [55] and focusing an ion beam in a neutralizing plasma to heat up targets began in 2009 on the NDCX I experiment at LBNL [56]. These experiments used 300–350 keV singly charged potassium ion beam, with a 30 A, 120 ns pulse section of the several microsecond pulse, that was compressed by a factor ∼60 to a 2 ns pulse. The velocity tilt was imparted by a separate induction buncher after a four solenoid transport section. A 1–2 m drift section followed during which plasma was injected by means of a ferro-electric plasma source. Four cathodic arc plasma sources, pointing upstream from beyond the final focus solenoid, supplied plasma into the solenoid and final focus region. Much of the several microsecond pre-pulse could be used to heat the ion beam because the hydrodynamic motion was not significant, until vaporization occurred. NDCX I has reached target temperatures of about 0.5 eV. The experiment is shown in Fig. 10.9.

A follow on experiment, NDCX II was designed [57, 58] to reach WDM conditions using the Bragg peak of Li. The design called for an ion energy of 2–3 MeV, and total charge of 0.03–0.06 μC in a compressed pulse 1 ns in duration. A CAD drawing of the experiment is shown in Fig. 10.10. The plan called for reusing the induction cores and other hardware including the pulse power systems from the decommissioned LLNL ATA accelerator. The NDCX II accelerator is under construction at the time of this writing.

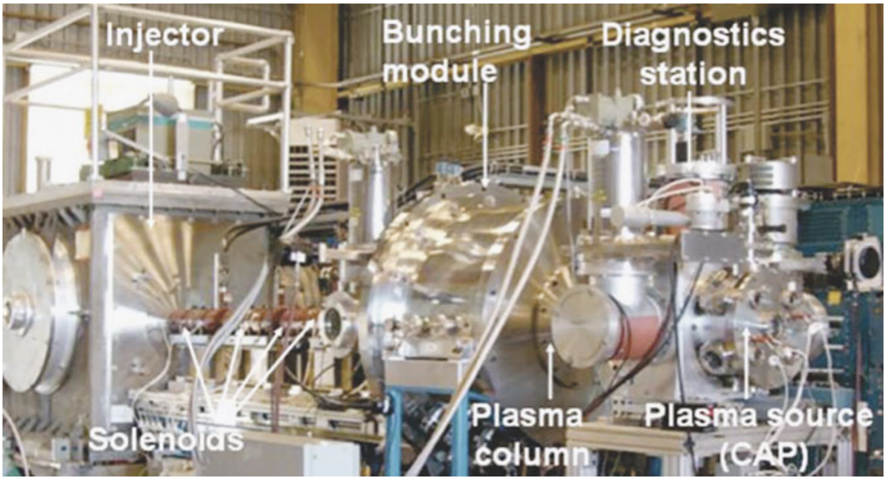

Fig. 10.9 The neutralized drift compression experiment (NDCX I) at LBNL in 2009

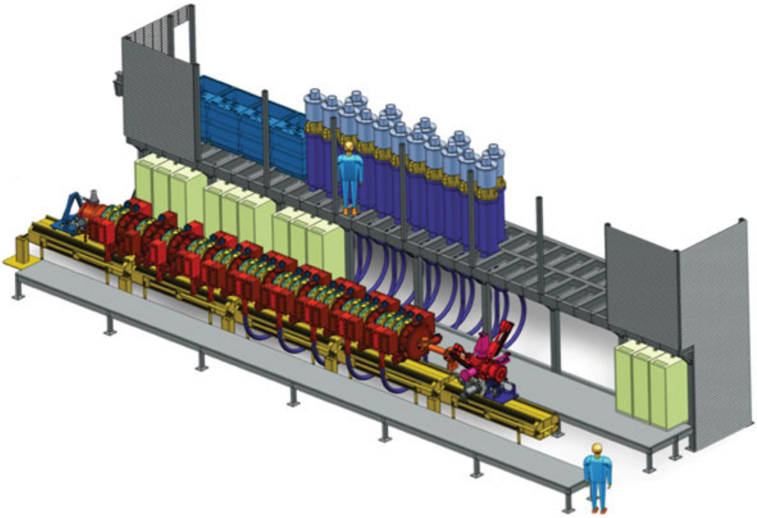

Fig. 10.10 A CAD drawing of the NDCX II experiment planned for completion at LBNL in 2012

10.2.2 Neutron Spallation Source

Neutron scattering science requires intense sources since the interaction of neutrons with matter is relatively weak. Research reactors have been used as sources for many years. The ILL reactor at Grenoble represents the most advanced capability, producing a neutron flux over 10^{15} $\mathrm{cm}^{-2}\mathrm{s}^{-1}$. With research reactors choppers are required to convert the continuous neutron flux into short pulses for time-of-flight separation into a monochromatic neutron beam. Pulsed accelerator-based spallation sources have now been shown to be viable options with significant advantages over reactors in the efficiency of neutron utilization and the avoidance of serious security and environmental protection issues. Indeed two major new facilities designed for average beam powers of order 1 MW are now beginning operation: the SNS in the USA [59] and J–PARC [60] in Japan. Both of these facilities are so-called "short pulse" (SP) spallation sources: a millisecond time scale negative ion beam from an RF linac is stacked in a storage ring and then extracted to deliver a sub-μs proton beam on a target. An alternate accelerator-based neutron source concept is the so-called "long pulse" (LP) spallation source. In this approach a few millisecond proton beam pulse is accelerated in an RF linac and sent directly to a target. The neutron pulse produced in the target can then be chopped to an even shorter duration (if desired) as in the reactor approach. This approach is currently being considered in Europe as the basis for a next generation spallation source that will deliver a time average neutron flux equivalent to the ILL reactor (the 5 MW ESS).

A short pulse spallation neutron source requires delivery of intense $\sim$1 GeV proton pulses of < 1 μs duration on a target at a typical repetition rate of 50–60 Hz. The fact that these parameters were a "natural fit" to the capabilities of induction linac technology was noted in the 1980s by Denis Keefe [61]. The relative "immaturity" of induction linac technology for accelerating protons at the GeV scale prevented its serious consideration as an option at that time. If induction technology began to be applied more widely, however, with some of the new applications discussed in this book, this situation might change at some time in the future.

The great disparity between the maturity of negative ion RF accelerators and storage rings, and ∼1 GeV induction accelerators operating at high CW power levels and accelerating protons, makes it difficult to do an honest comparison between the two for this application. On fundamental grounds, however, it would certainly seem probable that going through all the manipulations involved in accelerating a millisecond negative ion pulse in an RF accelerator, stripping and stacking them as protons in a storage ring, and extracting the protons in sub microsecond pulses will ultimately limit the scaling of this technical approach to higher powers cost effectively. In fact the intensity limitation on the number of protons per bunch in a storage ring is a serious constraint in the RF approach, and it appears to have been a major factor in the recent decision by the European ESS team to choose the LP approach for a 5 MW capability.

To illustrate the general parameter range involved, consider a 5 MW spallation source (a next generation facility like the ESS). Assuming 1 GeV protons (for efficient neutron production), 100 μ C pulses are required assuming a repetition rate of 50 Hz. As an example (not optimum necessarily), a single channel 3 T solenoid transport system can transport a proton line charge density of 2.6 μ C/m assuming a beam radius of 1.5 cm. The beam pulse length would then be 38 m through the accelerator. The injector would need to produce a 60 A, 1.6 μs proton beam pulse. These injector parameters are not unreasonable based on MFE neutral beam source developments in the 1980s, but this area clearly represents one of the developments that would be required. At the accelerator output, the pulse length would be about 160 ns and the current would be 600 amps. Note that the pulse length is less than a microsecond over most of the machine. The short pulse length and high beam current facilitate the design of high efficiency, high gradient induction cells, as in the HIF application.

Spallation sources do need to have very high reliability and availability to be accepted by the neutron scattering community. The beam transport also needs to be very low loss to avoid issues of remote handling and the associated costs. It therefore will likely remain the case that serious consideration of induction linacs in this application will not occur without significant demonstrations at an appropriate scale. There is obviously a high degree of synergism with the HIF system, so one avenue might be making the next major HIF experimental facility compatible with demonstrating proton beam acceleration as an SNS prototype.

References

1. Initial research on accelerators for heavy ion fusion can be found in the early workshops on the topic: ERDA summer study of heavy ions for inertial fusion, Lawrence Berkeley Laboratory, LBL-5543 (1976); Proceedings of the HIF Workshop, Brookhaven National Laboratory,

17 Oct., 1977, BNL-50769 (1977); Proceedings of the HIF Workshop, Argonne National Laboratory, 19–26 Sep., 1978, ANL-79-41 (1978); Proceedings of the HIF Workshop, Berkeley, CA, 29 Oct.–9 Nov., 1979, Lawrence Berkeley Laboratory, LBL-10301 (1980); Proceedings of more recent heavy ion fusion symposia can be found in: Particle Accelerators 37–38 (1992); Il Nuovo Cimento A 107 (1993); Fusion Engineering and Design 32–33 (1996); Nucl. Instr. Meth. A 415 (1998), 464 (2001), 544 (2005), 577 (2007) and 606 (2009).

2. I. Hofmann and G. Plass. (editor). The HIDIF-Study. Technical Report GSI-98-06, GSI, 1998.
3. J. Lindl. *Inertial Confinement Fusion: the Quest for Ignition and Energy Gain Using Indirect Drive*. Springer, New York, NY, 1998.
4. B. Logan, L. Perkins, and J. Barnard. Direct Drive Heavy-Ion-Beam Inertial Fusion at High Coupling Efficiency. *Phys. Plasmas*, 15:072701, 2008.
5. M. Tabak and D. Callahan-Miller. Design of a Distributed Radiator Target for Inertial Fusion Driven from Two Sides with Heavy Ion Beams. *Phys. Plasmas*, 5:1895, 1998.
6. D. Callahan-Miller and M. Tabak. Progress in target physics and design for heavy ion fusion. *Phys. Plasmas*, 7:2083, 2000.
7. D. Callahan, M. Herrmann, and M. Tabak. Progress in heavy ion target capsule and hohlraum design. *Laser Part. Beams*, 20:3:405–410, 2002.
8. D. Callahan, D. Clark, A. Koniges, M. Tabak, G. Bennett, M. Cuneo, R. Vesey, and A. Nikroo. Heavy-Ion Target Physics and Design in the USA. *Nucl. Inst. Meth. A*, 544:9–15, 2005.
9. B. Logan, R. Bangerter, D. Callahan, M. Tabak, M. Roth, L. Perkins, G. Caporaso. Assessment of Potential for Ion-Driven Fast Ignition. *Fusion Sci. Technol.*, 49, 399–411, 2006.
10. M. Reiser. *Theory and Design of Charged Particle Beams*, Wiley, New York, NY, 1994.
11. J. Barnard, A. Brooks, J. Clay, F. Coffield, F. Deadrick, L. Griffith, A. Harvey, D. Judd, H. Kirbie, V. Neil, M. Newton, A. Paul, L. Reginato, G. E. Russel, W. Sharp, H. Shay, J. Wilson, and S. Yu. Study of Recirculating Induction Accelerators as Drivers for Heavy Ion Fusion. Technical Report UCRL-LR-108095, Lawrence Livermore National Laboratory, 1991.
12. D. Neuffer. Geometric Aberrations in Final Focussing for Heavy Ion Fusion. Technical Report ANL-79-41, Argonne National Laboratory, 1978.
13. D. Ho, I. Haber, and K. Crandell. Octupole Correction of Geometric Aberrations for High-Current Heavy Ion Beams. *Part. Accel.*, 36:141–160, 1991.
14. D. Judd. Phase space constraints on some heavy-ion inertial-fusion igniters and example designs of 1 mj rf linac systems. Technical Report ANL-79-41, p. 237, Argonne National Laboratory, 1978.
15. D. Grote, A. Friedman, G. Craig, W. Sharp, and I. Haber. Progress Toward Source-to-Target Simulations. *Nucl. Instr. Meth. A*, 464:563, 2001.
16. J. Barnard, R. Bangerter, A. Faltens, T. Fessenden, A. Friedman, E. Lee, B. Logan, S. Lund, W. Meier, W. Sharp, and S. Yu. Induction Accelerator Architectures for Heavy Ion Fusion. *Nucl. Inst. Meth. A*, 415:218, 1998.
17. E. Lee. Solenoid Transport for Heavy Ion Fusion. *Nucl. Inst. Meth. A*, 544:187–193, 2005.
18. S. Yu, R. Abbott, R. Bangerter, J. Barnard, R. Briggs, D. Callahan, C. Celata, R. Davidson, C. Debonnel, S. Eylon, A. Faltens, A. Friedman, D. Grote, P. Heitzenroeder, E. Henestroza, I. Kaganovich, J. Kwan, J. Latkowski, E. Lee, B. Logan, P. Peterson, D. Rose, P. Roy, G.-L. Sabbi, P. Seidl, W. Sharp, and D. Welch. Heavy Ion Fusion (HIF) Driver Point Designs. *Nucl. Inst. Meth. A*, 544:294–299, 2005.
19. S. Yu, W. Meier, R. Abbott, J. Barnard, T. Brown, D. Callahan, C. Debonnel, P. Heitzenroeder, J. Latkowski, B. Logan, S. Pemberton, P. Peterson, D. Rose, G-L. Sabbi, W. Sharp, and D. Welch. An Updated Point Design for Heavy Ion Fusion. *Fusion Sci. Technol.*, 44:266–273, 2003.
20. S. Yu, J. Barnard, R. Briggs, D. Callahan, C. Celata, L. Chao, R. Davidson, C. Debonnel, S. Eylon, A. Friedman, E. Henestroza, I. Kaganovich, J. Kwan, E. Lee, M. Leitner, B. Logan, W. Meier, P. Peterson, L. Reginato, D. Rose, P. Roy, W. Waldron, and D. Welch. Towards a Modular Point Design for Heavy Ion Fusion. *Fusion Sci. Technol.*, 47:621–625, 2005.

21. T. Godlove. Heavy Ion Recirculating Induction Linac Studies. *Part. Accel.*, 37–38:439–451, 1992.
22. M. Reiser. Periodic Focusing of Intense Beams. *Part. Accel.*, 8:167–182, 1978.
23. M. G. Tiefenback. *Space-Charge Limits on the Transport of Ion Beams in a Long Alternating Gradient System*. PhD thesis, University of California at Berkeley, CA, 1986.
24. I. Hofmann, L. Laslett, L. Smith, and I. Haber. Stability of the Kapchinskij-Vladimirskij (K-V) Distribution in Long Periodic Transport Systems. *Part. Accel.*, 13:145–178, 1983.
25. S. Lund and S. Chawla. Space-Charge Transport Limits of Ion Beams in Periodic Quadrupole Focusing Channels. *Nucl. Inst. Meth. A*, 561:203–208, 2006.
26. R. Bangerter. The Induction Approach to Heavy-Ion Inertial Fusion: Accelerator and Target Considerations. *Il Nuovo Cimento*, 106:1445, 1993.
27. W. Meier, R. Bangerter, and A. Faltens. An Integrated Systems Model for Heavy Ion Drivers. *Nucl. Inst. Meth. A*, 415:249–255, 1997.
28. C. Celata. Scientific Issues in Future Induction Linac Accelerators for Heavy-Ion Fusion. *Nucl. Inst. Meth. A*, 544:142–150, 2005.
29. P. Seidl, C. Celata, A. Faltens, W. Fawley, W. Ghiorso, and S. Maclaren. Progress on the Scaled Beam Combining Experiment at LBNL. *Nucl. Inst. Meth. A*, 415:243–248, 1998.
30. J.-L. Vay, M. Furman, P. Seidl, R. Cohen, A. Friedman, D. Grote, M. Kireeff Covo, A. Molvik, P. Stoltz, S. Veitzer, and J. Verboncoeur. Studies of the Physics of Space-Charge-Dominated Beams for Heavy Ion Inertial Fusion. *Nucl. Inst. Meth. A*, 577, 2007.
31. A. Molvik, M. Kireeff Covo, R. Cohen, A. Friedman, S. Lund, W. Sharp, J.-L. Vay, D. Baca, F. Bieniosek, C. Leister, and P. Seidl. Quantitative Experiments with Electrons in a Positively Charged Beam. *Phys. Plasmas*, 14:056701, 2007.
32. W. Fawley, T. Garvey, S. Eylon, E. Henestroza, A. Faltens, T. Fessenden, K. Hahn, L. Smith, and D. Grote. Beam Dynamics Studies with the Heavy-Ion Linear Induction Accelerator MBE-4. *Phys. Plasmas*, 4:880, 1997.
33. B. Logan. Exploring a Unique Vision for Heavy Ion Fusion. Technical Report HIFAN, Lawrence Berkeley Laboratory, 2008.
34. T. Sangster, J. Barnard, T. Cianciolo, G. Craig, A. Friedman, D. Grote, E. Halaxa, R. Hanks, G. Kamin, H. Kirbie, B. Logan, S. Lund, G. Mant, A. Molvik, W. M. Sharp, S. Eylon, D. Berners, T. Fessenden, D. Judd, L. Reginato, H. Hopkins, A. Debeling, W. Fritz, and J. Meredith. Status of Experiments Leading to a Small Recirculator. *Nucl. Inst. Meth. A*, 415:310–314, 1998.
35. L. Ahle, T. Sangster, D. Autrey, J. Barnard, G. Craig, A. Friedman, D. Grote, E. Halaxa, B. Logan, S. Lund, G. Mant, A. Molvik, W. Sharp, S. Eylon, A. Debeling, and W. Fritz. Current Status of the Recirculator Project. In *Proceedings of the 1999 Particle Accelerator Conference*, pages 3248–3250, New York, NY, 29 March–2 April 1999.
36. R. Kishek, S. Bernal, Y. Cui, T. Godlove, I. Haber, J. Harris, Y. Huo, H. Li, P. O'Shea, B. Quinn, M. Reiser, M. Walter, M. Wilson, and Y. Zou. HIF Research on the University of Maryland Electron Ring (UMER). *Nucl. Inst. Meth. A*, 544:179–186, 2005.
37. J. Wang, S. Bernal, P. Chin, T. Godlove, I. Haber, R. Kishek, Y. Li, M. Reiser, M. Venturini, R. York, and Y. Zou. Studies of the Physics of Space-Charge-Dominated Beams for Heavy Ion Inertial Fusion. *Nucl. Inst. Meth. A*, 415, 1998.
38. C. Celata, F. Bieniosek, and A. Faltens. Transverse Splitting of Intense Heavy-Ion Beams in the IRE and in an HIF Driver. *Nucl. Inst. Meth. A*, 464:533–538, 2001.
39. National Research Council Committee on High Energy Density Physics, Plasma Science Committee. *Frontiers in High Energy Density Physics: the X-Games of Contemporary Science*. National Academies Press, Washington, DC, 2003.
40. National Task Force on High Energy Density Physics. Frontiers for Discovery in High Energy Density Physics. Office of Science and Technology Policy, National Science and Technology Council Interagency Working Group on the Physics of the Universe, 2004.
41. R. More, H. Yoneda, and H. Morikami. Short Pulse Lasers and Electron Dynamics in Warm Dense Matter. *J. Quant. Spectros. Radiat. Trans.*, 99:409–424, 2006.

42. T. Guillot. The Interiors of Giant Planets: Models and Outstanding Questions. *Annu. Rev. Earth Planet. Sci.*, 33:493–530, 2005.
43. N. Tahir, A. Shutov, I. Lomonosov, A. Piriz, G. Wouchuk, C. Deutsch, D. Hoffmann, and V. Fortov. Numerical Simulations and Theoretical Analysis of High Energy Density Experiments at the Next Generation of Ion Beam Facilities at Darmstadt: The Hedgehob Collaboration. *High Energy Density Phys.*, 2:21–34, 2006.
44. J. Barnard, P. Seidl, J. Coleman, and D. Ogata. Estimates of Energy Fluence at the Focal Plane in Beams Undergoing Neutralized Drift Compression. In *Proceedings of the 2008 Linear Accelerator Conference*, page MOP031, Victoria, Canada, 28 Sept.–3 Oct. 2008.
45. L. Northcliffe and R. Schilling. Range and Stopping-Power Tables for Heavy Ions. *Nucl. Data Tables*, A7:233, 1970.
46. L. Grisham. Moderate Energy Ions for High Energy Density Physics Experiments. *Phys. Plasmas*, 11:5727, 2004.
47. L. Landau and E. Lifshitz. *Fluid Mechanics*. Pergamon Press, New York, NY, 1959. see Chapter 10.
48. R. Harrach and F. Rogers. Comparison of Two Equation-of-State Models for Partially Ionized Aluminum: Zeldovich and Raizer's Model Versus the Activity Expansion Code. *J. Appl. Phys.*, 52:5592, 1981.
49. S. Atzeni and J. Meyer ter Vehn. *The Physics of Inertial Fusion: Beam Plasma Interaction, Hydrodynamics, Hot Dense Matter*. Oxford University Press, Inc, New York, NY, 2004.
50. J. Barnard, R. Briggs, D. Callahan, R. Davidson, A. Friedman, L. Grisham, E. Lee, R. Lee, B. Logan, C. Olson, D. Rose, P. Santhanam, A. Sessler, J. Staples, M. Tabak, D. Welch, J. Wurtele, and S. Yu. Accelerator and Ion Beam Tradeoffs for Studies of Warm Dense Matter. In *Proceedings of the 2005 Particle Accelerator Conference*, pages 2568–2570, Knoxville, TN, 16–20 May 2005.
51. D. Welch, J. Coleman, P. Seidl, P. Roy, E. Henestroza, E. Lee, A. Sefkow, E. Gilson, T. Genoni, and D. Rose. Source-to-Target Simulation of Simultaneous Longitudinal and Transverse Focusing of Heavy Ion Beams. *Phys. Rev. Special Topics – Accelerators and Beams*, 11, 2008.
52. A. Sefkow, R. Davidson, I. Kaganovich, E. Gilson, P. Roy, P. Seidl, S. Yu, D. Welch, D. Rose, and J. Barnard. Optimized Simultaneous Transverse and Longitudinal Focusing of Intense Ion Beam Pulses for Warm Dense Matter Applications. *Nucl. Inst. Meth. A*, 577:289–297, 2007.
53. I. Kaganovich, R. Davidson, M. Dorf, E. Startsev, A. Sefkow, J. Barnard, A. Friedman, E. Lee, S. Lidia, B. Logan, P. Roy, P. Seidl, and D. Welch. Designing Neutralized Drift Compression for Focusing of Intense Ion Beam Pulses in Background Plasma. In *Proceedings of the 2009 Particle Accelerator Conference*, page TH3GA103, Vancouver, Canada, 4–8 May 2009.
54. F. Bieniosek, E. Henestroza, M. Leitner, B. Logan, R. More, P. Roy, P. Ni, P. Seidl, W. Waldron, and J.Barnard. High-Energy Density Physics Experiments with Intense Heavy Ion Beams. *Nucl. Inst. Meth. A*, 606:146–151, 2009.
55. P. Roy, S. Yu, E. Henestroza, A. Anders, F. Bieniosek, J. Coleman, S. Eylon, W. Greenway, M. Leitner, B. Logan, W. Waldron, D. Welch, C. Thoma, A. Sefkow, E. Gilson, P. Efthimion, and R. Davidson. Drift Compression of an Intense Neutralized Ion Beam. *Phys. Rev. Lett.*, 95:234801, 2005.
56. P. Seidl, A. Anders, F. Bieniosek, J. Barnard, J. Calanog, A. Chen, R. Cohen, J. Coleman, M. Dorf, E. Gilson, D. Grote, J. Jung, M. Leitner, S. Lidia, B. Logan, P. Ni, P. Roy, K. Van den Bogert, W. Waldron, and D. Welch. Progress in Beam Focusing and Compression for Warm-Dense Matter Experiments. *Nucl. Inst. Meth. A*, 606:75–82, 2009.
57. A. Friedman, J. Barnard, R. Briggs, R. Davidson, M. Dorf, D. Grote, E. Henestroza, E. Lee, M. Leitner, B. Logan, A. Sefkow, W. Sharp, W. Waldron, D. Welch, and S. Yu. Toward a Physics Design for NDCX-II, an Ion Accelerator for Warm Dense Matter and HIF Target Physics Studies. *Nucl. Inst. Meth. Phys. Res. A*, 606:6–10, 2009.
58. A. Friedman, J. Barnard, R. Cohen, D. Grote, S. Lund, W. Sharp, A. Faltens, E. Henestroza, J.-Y. Jung, J. Kwan, E. Lee, M. Leitner, B. Logan, J.-L. Vay, W. Waldron, R. Davidson,

M. Dorf, E. Gilson, and I. Kaganovich. Beam Dynamics of the Neutralized Drift Compression Experiment-II, a Novel Pulse-Compressing Ion Accelerator. *Phys. Plasmas*, 17:056704, 2010.

59. S. Henderson. Spallation Neutron Source Progress, Challanges and Upgrade Options. In *Proceedings of the 2008 European Particle Accelerator Conference*, page 2892, Genoa, Italy, 23–27 June 2008.
60. M. Kinsho. J-PARC Progress and Challanges of Protron Synchrotrons. In *Proceedings of the 2008 European Particle Accelerator Conference*, page 2897, Genoa, Italy, 23–27 June 2008.
61. D. Keefe and E. Hoyer. Proton Induction Linacs as High-Intensity Neutron Sources. Technical Report LBL-12855; CONF-8106120-4, Lawrence Berkeley Lab, 1981.